energies

MDPI

Article

Comprehensive Performance Evaluation of a Dual-Function Active Solar Thermal Façade System Based on Energy, Economic and Environmental Analysis in China

Rui Li and Guomin Cui *

School of Energy and Power Engineering, University of Shanghai for Science and Technology, Shanghai 200093, China; ruilee@usst.edu.cn
* Correspondence: cgm@usst.edu.cn

Abstract: Promoting the development and utilization of solar energy is a practical way to alleviate the energy crisis and achieve the goal of carbon neutrality. Recently, interest has arisen in the dual-functional active solar thermal façade (ASTF) system that produces hot water throughout the whole year and reduces cooling and heating load as a function of the building façade. Here, a mathematical model of the ASTF system is built and validated by the experimental data, and the annual performance of the ASTF system in representative cities in three climate regions is evaluated. The results are that compared with the common solar water system, the ASTF system adds passive energy savings, which accounts for 5.8%, 7.2% and 11.4% of the total primary energy savings of the system for Shanghai, Beijing and Lanzhou. Compared with the traditional wall, the ASTF saves 16.4% and 23.0% of cooling energy consumption and 102.3% and 92.4% of heating energy consumption for Shanghai and Beijing, respectively. Additionally, it saves 74.7% of heating energy consumption for Lanzhou. Lastly, the impact of the design parameters and operation parameters of the system are investigated, respectively. This study demonstrates a viable path to promoting cost-effective active solar thermal façades in different climates, and the results can be beneficial to further research.

Keywords: active solar thermal façade; comprehensive evaluation; primary energy consumption; life-cycle saving

Citation: Li, R.; Cui, G. Comprehensive Performance Evaluation of a Dual-Function Active Solar Thermal Façade System Based on Energy, Economic and Environmental Analysis in China. *Energies* **2022**, *15*, 4147. https://doi.org/10.3390/en15114147

Academic Editors: Fei Cao and Yan Yang

Received: 19 April 2022
Accepted: 19 May 2022
Published: 5 June 2022

1. Introduction

Building energy consumption accounts for about a quarter of the world's energy consumption [1], and the proportion will increase to 35% by 2040 [2]. In China, buildings are responsible for 21.11% of the total society's energy consumption and 19.5% of the total society's CO_2 emissions [3]. Among building energy consumption, air conditioning and heating account for 55% in China. Among these, the heat loss of the envelope accounts for 70~80%, and the heat loss of the outer façade accounts for about 25% [4]. Expanding green energy utilization and reducing building energy consumption are the two main approaches to achieving carbon neutrality in the buildings sector. Thus, expanding the application of solar energy, the most easy-use and clean energy, is a useful way to alleviate the severe energy and environmental crisis.

The active solar thermal façade (ASTF) module based on the flat-plate solar thermal collector has been proved to be feasible and efficient to integrate with buildings [5–8] and plays an important role in the production of domestic hot water [9,10]. The ASTF has the heat collecting function of conventional solar thermal collectors, but it is different in architecturally acceptable structural design, safety installation and easy maintenance. Therefore, it has dual functions, both as a building façade and as a heat collecting component. As a building façade, it reduces heating load by shielding and insulation, decreases cooling load by removing heat gain through water circulation and extends solar applications in buildings. As the solar collecting component, the ASTF module collects without taking extra

space and transfers and stores solar energy for various uses in buildings which alleviates the pressure of energy and the environment. Furthermore, the ASTF module is easier to customize and produce, making it easy to integrate with the building.

In order to integrate the ASTF module with the building façade organically, substantial studies explore different types of collectors, improving their shapes and materials to make them more architecturally acceptable. Additionally, the research focus is mainly on the thermal efficiency of the ASTF system. In terms of collector types based on the ASTF module, in addition to flat-plate collectors, evacuated tube collectors and compound parabolic concentrator collectors are also used to integrate with buildings. Wu et al. [11] compared four solar façade (integrated with evacuated tube collector) cooling systems in solar fraction and unit cooling cost. Lamnatou et al. [12] proposed a vacuum-tube/BIST system and compared the gutter-integrated vacuum-tube system with the gutter-integrated flat-plate/BIST system from the perspective of life-cycle environment protection. The authors obtained the results that the energy payback time is 0.5 and 1.8 years for the system, respectively. Deng and Chen [5] proposed a novel embedded building evacuated tube collector coupled with a compound parabolic concentrator (CPC) system, suitable for integrating into building vertical façades. The authors determined an optical efficiency of 64.5% and average thermal efficiency of 51.4%. Harmin et al. [13] studied a solar water heater equipped with a linear parabolic reflector, integrating it into a building façade experimentally and numerically, and obtained the results that the mean daily efficiency of the water heater varies between 36.4% and 51.6% and the thermal losses coefficient of the reflector during night-time varies between 2.17 W/K and 3.12 W/K. In terms of the ASTF module shapes, triangular collector modules and modules with the same shape as specific parts of the building have been studied. Visa et al. [7] developed and optimally designed a novel triangle shape flat plate solar thermal collector to improve its architectural acceptance and obtained efficiencies of 55%, 42% and 35% of the collector with black, green and orange absorber plates through a test, respectively. Motte et al. [14] proposed and constructed a new solar thermal collector integrated into a gutter to recover rainwater and solar radiation and studied its thermal performance. In terms of the materials of the ASTF module: O'Hegarty et al. [15] studied the economical and durable concrete solar collector to seamlessly integrate it with the existing concrete wall and increased the outlet fluid temperatures up to 40 °C and the daily efficiency to 56%, which shows its competitiveness compared with the unglazed solar collector. Ibrahim et al. [8] proposed an active embedded-pipe envelope system to harvest solar energy and enhance thermal comfort. The comparative experimental study shows that the system performs very well in Mediterranean climates. Jia et al. [16] studied the textile-based solar thermal collectors numerically and experimentally, and their conclusion is that they can be widely used in low and medium temperature applications. Yang et al. [17] studied the all-ceramic flat plate solar collector with the characteristics of low cost and the same long lifetime as the building, and the thermal efficiency of the collector was 47.1% and 50% when it acted as balcony railings and integrated with building roof, respectively. Mertin et al. [18] presented a colored solar thermal collector with a thin-film coating on the reverse side of the glass and found an energy loss of only 2.8–4.5% at a normal solar incidence of the collector in comparison to uncoated glass panels.

In recent years, the thermal performance of the ASTF as a building wall has become the interest of researchers. Tomas et al. [19] studied façade-integrated solar collectors for hot water supply and obtained the results that building behavior is not strongly affected by façade collectors if sufficient insulation layers are present. Ji et al. [20] investigated the yearly performance of façade-integrated photovoltaic/thermal collector systems integrated into buildings in Hong Kong and found that the indoor heat gain was decreased when compared with conventional concrete walls.

These studies highlight the impressive developments made in recent years in the design progress and performance study of the ASTF system. However, limited attention has been paid to the comprehensive performance of the ASTF system, as its passive

energy-saving performance interacts with its active solar energy collecting performance. Furthermore, the economic and environmental performance of the ASTF should be calculated to determine the feasibility of its application in various climate areas.

In this study, inspired by the double advantages of the ASTF system, we mainly focus on the economic, energy-saving and environmental performance of the ASTF and explore the possibility of its application in different areas. Firstly, the energy balance of the ASTF system was analyzed to investigate the comprehensive performance considering both the performance of the ASTF and the ASTF system. Secondly, the annual performance of the ASTF in selected areas was obtained and compared with a traditional wall. Thirdly, the influence of parameters such as the tank volume to collector ratio, the control condition and the insulation thickness on its performance were discussed to find the optimum design. The results of this work can guide the proper application of the ASTF system in different climate areas.

2. Methodology and Data

2.1. Building Model and the ASTF System Configuration

The proposed ASTF modules, reformed based on a flat plate solar collector, were installed on the wall and roof of a standalone house. As is shown in Figure 1, the ASTF module consists of a transparent glass sheet, an absorption plate, pipes, insulation and aluminum alloy frames. Table 1 show the physical and thermal properties of the module.

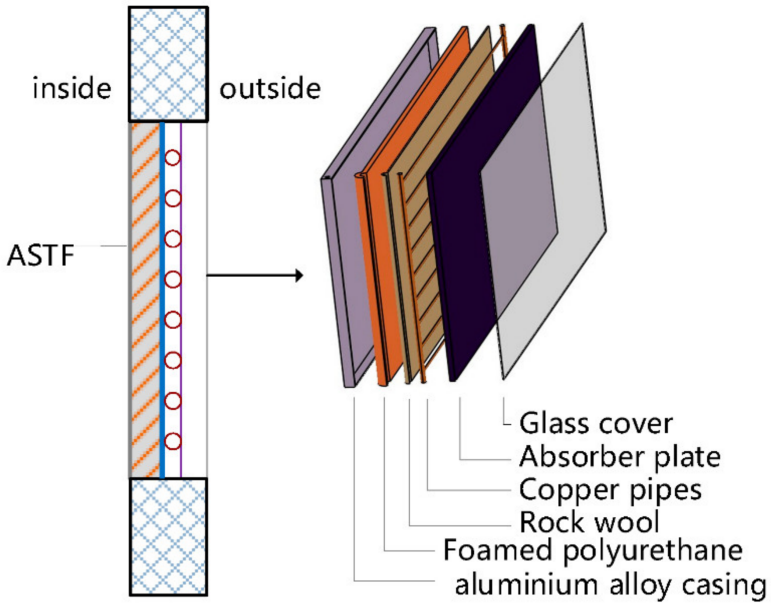

Figure 1. Structure of the ASTF module.

Table 1. Thermo-physical properties of different layers of the ASTF module.

Components	Parameters	Values	Units
Glass cover	Thermal capacity	790	J/(kg·k)
	Density	2600	kg/m^3
	Thermal conductivity	1.1	W/(m·K)
	Absorptivity	0.01	-
	Emissivity	0.84	-
	Transmittance	0.96	-
Absorber plate	Thermal capacity	880	J/(kg·k)
	Density	2700	kg/m^3
	Thermal conductivity	237	W/(m·K)

Table 1. *Cont.*

Components	Parameters	Values	Units
Tube	Absorptivity	0.95	-
	Emissivity	0.18	-
	Thermal capacity	390	J/(kg·k)
	Density	8900	kg/m^3
	Thermal conductivity	401	W/(m·K)
Insulation	Thermal capacity	1670	J/(kg·k)
	Density	37	kg/m^3
	Thermal conductivity	0.025	W/(m·K)
	Emissivity	0.9	-

In addition to the ASTF modules, the ASTF system components include a storage tank, water pumps, expansion tank, pipes and fan coil units, as is shown in Figure 2. Solar radiation is absorbed by the absorbing plate, and the heat is taken away by the fluid medium to the storage tank.

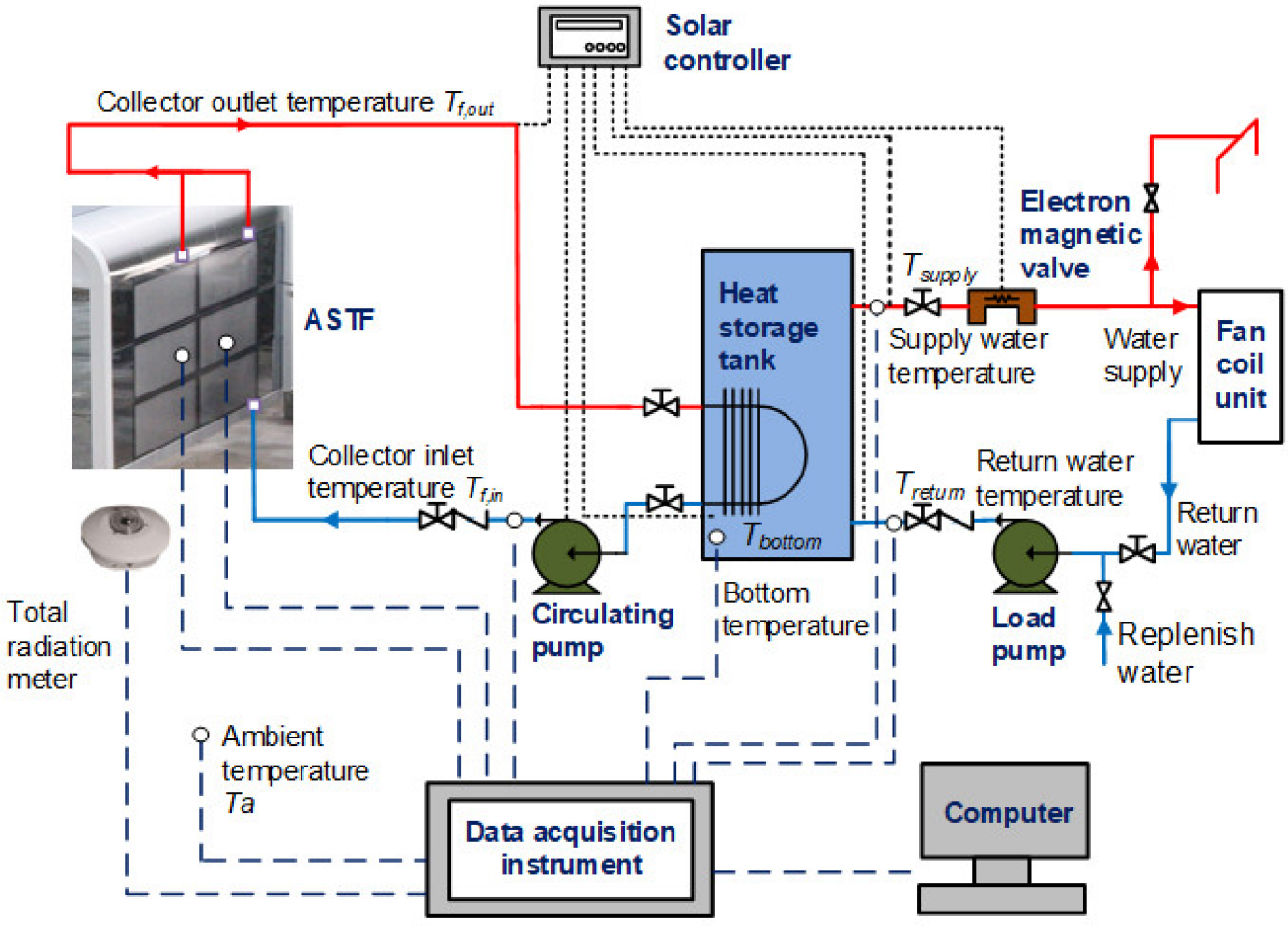

Figure 2. Schematic diagram of the ASTF system.

When supplying heat for the building, the hot water is forced to the fan-coil units to heat the indoor air circulating through the fan-coils. If the outlet water temperature of the storage is more than 50 °C and the temperature difference between supply and return is more than 5 °C, the pumps keep running. If that temperature difference drops to 3 °C, the pumps will be switched off. The main parameters of the ASTF system are listed in Table 2.

Table 2. Main parameters of the ASTF system.

Parameters		Value
Thickness(m)	cover	0.003
	Absorb plate	0.003
	Air gap	0.018
	Insulation	0.025
Inner/outer diameter of tube(m)		0.009/0.010
Tube spacing (m)		0.115
Tube length(m)		1.795
Collector area (m^2)		1686(0.885 m × 1.905 m)
Number of modules		6
Storage tank volume (m^3)		0.5
Mass flow rate (kg/s)		0.12
ON/OFF Control (heating collecting)		10 °C/4 °C
Slope		90°

2.2. Energy Balance Analysis of the ASTF System

In order to explain the basic working principle clearly and figure out the determining factor of thermal performance, the energy balance of the ASTF system is analyzed.

For the glass cover of the ASTF module, converting the solar radiation and conducting convection and radiation heat transfer with the surroundings, the energy balance equation can be given as [21–23]:

$$\delta_g \rho_g C_g \frac{dt_g}{d\tau} = G_t \alpha_g + h_{c,g-a}(t_a - t_g) + \varepsilon_g \sigma\left(t_s^4 - t_g^4\right) + h_{c,g-p}(t_p - t_g) + \frac{\sigma\left(t_p^4 - t_g^4\right)}{\frac{1}{\varepsilon_p} + \frac{1}{\varepsilon_g} - 1} \quad (1)$$

For the absorbing plate of the ASTF module, transferring the solar energy to the flow medium in the copper tube and conducting convection and radiation heat transfer with the glass cover and the insulation layer, the energy balance equation can be expressed as:

$$\delta_p \rho_p C_p \frac{dt_p}{d\tau} = G_t(\tau_c \alpha_p) - h_{c,g-p}(t_p - t_g) - \frac{\sigma\left(t_p^4 - t_g^4\right)}{\frac{1}{\varepsilon_p} + \frac{1}{\varepsilon_g} - 1} - h_{c,p-ins}\,(t_p - t_{ins}) + \delta_p \lambda_p \frac{d^2 t_p}{dz^2} \quad (2)$$

where $\left.\frac{dt_p}{dz}\right|_{z=0} = 0$ and $\left.\frac{dt_p}{dz}\right|_{z=\frac{W_o - D_o}{2}} = h_{p-f}\left(t_f - t_p\right)$.

For the heat transfer flow medium in the tube, when the pump is on, the solar gain from the absorbing plate is mostly taken away by the flow medium as in Equation (3), and when the pump is off, the solar gain from the absorb plate mostly results in the temperature rise of the water medium in the tube as in Equation (4) [24]:

$$\left(\frac{D_i}{2}\right)^2 \rho_f C_{p,f} \frac{dt_f}{d\tau} = D_e h_{p-f}\left(t_p - t_f\right) - \left(\frac{D_i}{2}\right)^2 \nu_f \rho_f C_{p,f} \frac{dt_f}{dy} \quad (3)$$

$$\left(\frac{D_i}{2}\right)^2 \rho_f C_{p,f} \frac{dt_f}{d\tau} = D_o h_{p-f}\left(t_p - t_f\right) \quad (4)$$

For the insulation layer, integrated with the aluminum backplate and carried heat transfer with the absorbing plate and the indoor environment, the energy balance equation is as follows [25,26]:

$$\rho_{ins} C_{ins} \frac{\partial t_{ins}}{\partial \tau} = \lambda_{ins} \frac{\partial^2 t_{ins}}{\partial x^2} \quad (5)$$

where $-\lambda_{ins}\left(\frac{\partial t_{ins}}{\partial x}\right)\Big|_{x=0} = (h_{c,ins-i} + h_{r,b-i})(t_{ins} - t_i)$ and $t_{ins}\big|_{x=\delta_{ins}} = t_p$.

For the storage tank, assuming the heat transfer is unidimensional and the properties are invariant, the energy balance equation can be given as:

$$V_{st}\rho_f C_{p,f}\frac{\partial t_{st}}{\partial \tau} = C_{p,f}M\left(t_{f,out} - t_{f,in}\right) - (UA)_{st}(t_{st} - t_a) \quad (6)$$

Tests on the south façade were from 08:00 to 18:00, which is the working time and air conditioning system running time. Resistance thermometers (±0.1 °C accuracy) were placed at the inlet and outlet of the ASTF module to measure the water temperature, outside the façade to measure the outdoor air temperature, in the house to measure the indoor temperature, and at the internal and external surface of the façade to the measure the surface temperatures. An ultrasonic flow meter (1–5% accuracy) was used to test the water flow rate in the heat collecting cycle and heat supply cycle. A TBQ-2 radiometer (absolute error of 1 W/m^2) was installed on the surface of the façade to monitor the solar radiation value at the vertical surface.

RMSD (root mean square deviation) is used to assess the reliability of the theoretical model. The RMSD can be obtained from the following formula.

$$RMSD = \sqrt{\frac{\sum\left[\left(t_{experimental} - t_{simulated}\right)/t_{experimental}\right]^2}{n}} \times 100\% \quad (7)$$

According to the experimental results [27], comparison of temperatures and efficiency between experiment and simulation is displayed in Figure 3. It is easy to notice that the observations certainly back up the models. The RMSD of the internal surface temperature (t_w), the external wall surface temperature (t_g) and the outlet water temperatures ($t_{f,out}$) are 1.0 °C, 1.1 °C and 3.0 °C, respectively. Analyzing the experiment and simulation data, the experimental average daily efficiency is 56%, while the simulated value is 53.1%, with a deviation of 2%. Therefore, the validity of the energy balance model and method can be proved by the experimental data.

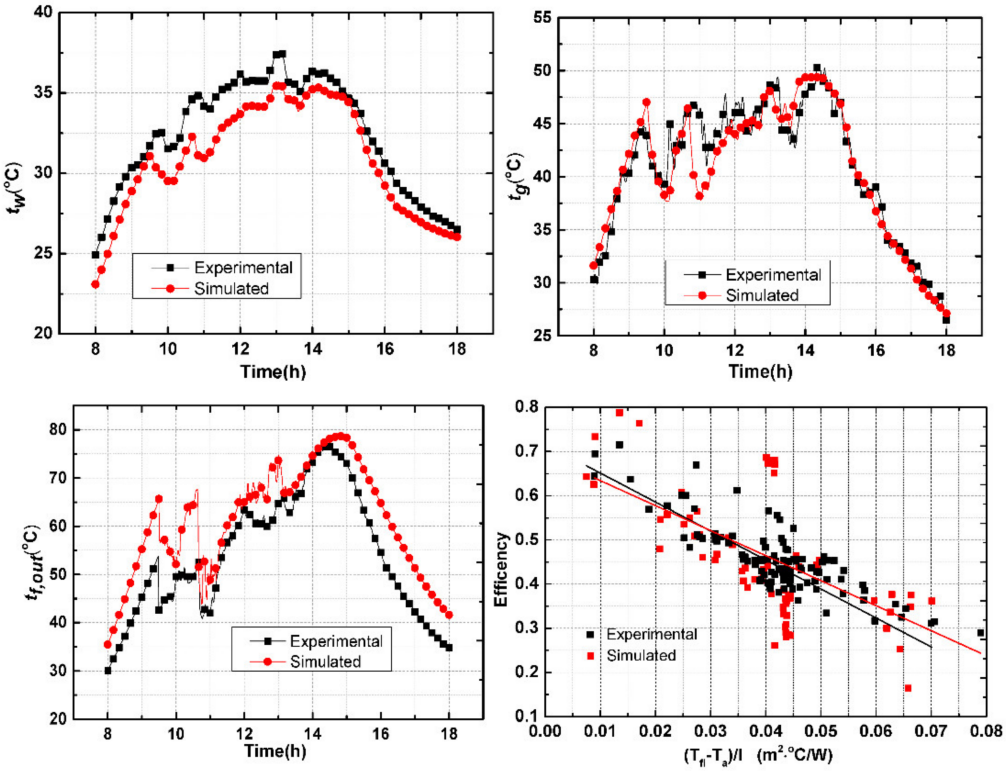

Figure 3. Comparison of temperatures and efficiency between experiment and simulation.

2.3. Comprehensive Evaluation

(1) Energy evaluation

The thermal performance of the ASTF is characterized by daily or monthly total cooling or heating transmission loads, which can be obtained from the solution as:

$$Q_d = \int_0^{24h} h_{wi}(t_b - t_i)d\tau \quad (8)$$

$$Q_m = \int_0^{m} h_{wi}(t_b - t_i)d\tau \quad (9)$$

where t_b is inner wall temperature; t_i is the indoor temperature. Notably, both values of Q_d and Q_m are added separately for cooling and heating.

The annual performance of the ASTF system can be reflected by its monthly mean thermal efficiency, which can be calculated by Equation (10).

$$\eta_m = \frac{Q_u}{A_c I_t} = \frac{C_p \int_0^m \dot{M}(t_{f,out} - t_{f,in})}{A_c \int_0^m I_t} \times 100\% \quad (10)$$

To further explore the energy performance of the ASTF system, a conventional system comprised of an electrically driven vapor compression refrigerator and a gas water heater is selected as a reference system to compare with it. As the ASTF system produces thermal energy in an active way and influences the HVAC energy demand in a passive way, the prime energy saving (*PES*) is proposed as a comprehensive indicator to evaluate the energy-saving potential of the system. It can be expressed as:

$$PES = \varepsilon_{gas}\left(\frac{Q_u}{\eta_{gas}} + \frac{Q_{h,REF-}Q_{h,ASTF}}{\eta_{gas}}\right) + \varepsilon_{ele}\left(\frac{Q_{c,REF-}Q_{c,ASTF}}{COP_{c,REF}}\right) \quad (11)$$

where ε_{gas} and ε_{ele} are primary energy conversion factors of gas and electricity, and in this paper their values are 1.22 and 3.07 [28], respectively.

(2) Economic evaluation

In this paper, the economic performance of the ASTF system was assessed based on the life-cycle savings, which are defined as the difference between the life cycle cost of a conventional wall with conventional systems and the life cycle cost of the ASTF system. The expression is as follows:

$$LC = (C_{gas}\Delta E_{gas} + C_{ele}\Delta E_{ele})PWF - \Delta I_{OM}PWF - \Delta I_{system} \quad (12)$$

where $\Delta E_{gas} = (Q_u + \Delta Q_h)/\eta_{gas}$ is the saving energy of hot water; CV_g is the calorific value of gas; η_g is the comprehensive efficiency of a gas water heater; c_g is gas price; c_{ele} is electricity price; $\Delta E_{ele} = \Delta Q_c/COP_{c,REF}$ is electricity saving of heating and cooling; ΔI_{system} is increased investment in the system; ΔI_{OM} is increased operation and maintenance cost;

The net present value (NPV) at the time of the Yth year is defined as the Y year savings, which are the difference between the Y year cost of a conventional wall with conventional systems and the Y year cost of the ASTF system.

PWF is the present worth factor which brings the future cost into the present time. Based on the formula [29], the *PWF* considering the rise of fuel prices can be expressed as:

$$PWF(n, r_i, r_d, r_r) = \sum_{j=1}^{n} \frac{(1 + r_i)^{j-1}(1 + r_r)^{j-1}}{(1 + r_d)^j} = \frac{1}{(r_d - r_i - r_r - r_i r_r)}[1 - \frac{(1 + r_i)^n(1 + r_r)^n}{(1 + r_d)^n}] \quad (13)$$

where n is lifetime; r_d is the discount rate; r_i is inflation rate; r_r is the real floating interest rate.

The main parameters for the economic analysis and capital cost are shown in Tables 3 and 4.

Table 3. Parameters used in the economic analysis [30].

Parameter	Unit	Value
Average inflation rate (r_i)	%	2.9
Interest rate (discount rate) (r_d)	%	6
Real floating interest rate of gas price ($r_{r,gas}$)	%	2
Real floating interest rate of electricity price ($r_{r,ele}$)	%	3
Average electricity price (c_{ele})	Yuan/kWh	0.6
Average gas price (c_{gas})	Yuan/GJ	90
Life of the ASTF system (n)	Year	20
Maintenance cost of the ASTF system	% of capital cost	1.25
Installation cost of the ASTF cost	% of capital cost	5

Table 4. Capital cost the ASTF system.

Components	Initial Investment (Yuan)
ASTF module	$Z_{ASTF} = 500A_{ASTF}$
Water tank	$Z_{st} = 531.9V_{st} + 1156.8$
Heat exchanger	$Z_{ex} = 1574(A_{ex})^{0.4162}$
Pump	$Z_{pump} = 66.9\,m + 103.8H + 950.8$
Controller	$Z_{ctrl} = 100$

(3) CO_2 emission reduction

The impact of the ASTF system on the environment should be considered to deal with the increasingly severe environmental problems. And in order to cope with climate change, China has set the goal of reaching the peak of carbon emission by 2030 and achieving carbon neutrality by around 2060. Therefore, CO_2 emission is a major indicator. The annual CO_2 emissions can be obtained from the following equation:

$$\Delta CE_{CO_2} = \Delta E_{ele} \cdot e_{CO_2,ele} + \Delta E_{gas} \cdot e_{CO_2,gas} \cdot kg_{CO_2}/year \quad (14)$$

where $e_{CO_2,ele}$ and $e_{CO_2,gas}$ are the CO_2 emission factors of electricity and natural gas, which are 756 kg_{CO_2}/MWh and 184 kg_{CO_2}/MWh, respectively.

2.4. Selected Climates

In order to analyze the viability of the ASTF under various climatic conditions, three cities, Shanghai, Beijing and Lanzhou, with different climates, are selected to study. Table 5 present solar irradiation on the south-facing façade of three cities.

Table 5. Climate data for the three cities [31].

	Shanghai	Beijing	Lanzhou
Location	N 30°40′–31°53′	N 39°26′–41°03′	N 35°23′–N 37°42′
Climate	Subtropical monsoon	Semi humid continental monsoon	Temperate continental
Annual irradiation on south facing façade	3125.2 MJ/m^2	3909.2 MJ/m^2	3789.1 MJ/m^2
Heat degree days	1648	2470	2766

Figure 4 display the annual distribution of solar radiation on the south-facing façade.

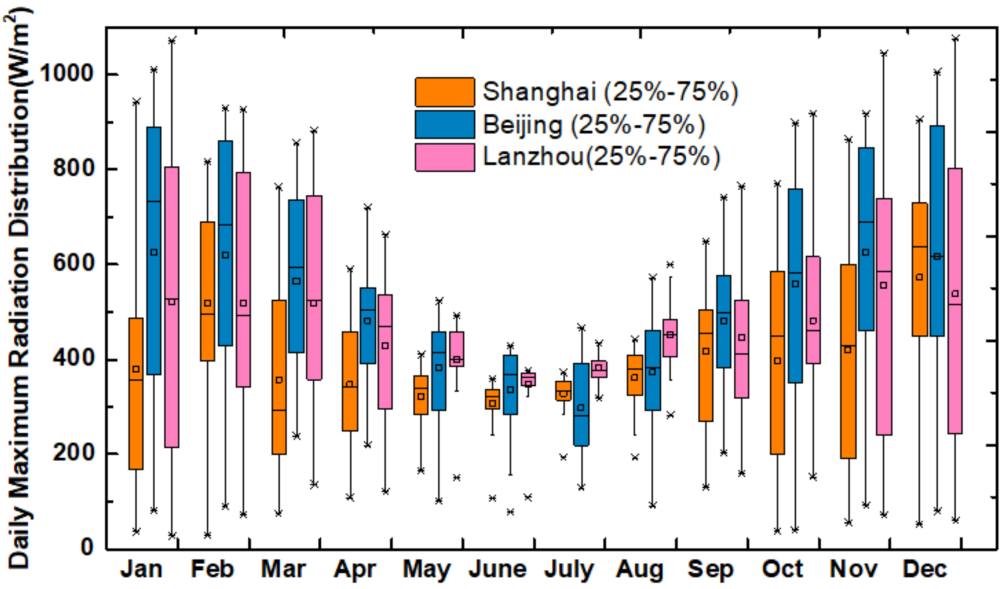

Figure 4. Monthly distribution of daily maximum radiation for the three cities.

3. Results and Discussion

3.1. Yearly Thermal Performance of the ASTF System in the Typical Cities

The cooling and heating seasons of the three cities are different because they are in different climatic zones. In Shanghai, the heating season is from January to March and from November to December, and the cooling season is from June to August. In Beijing, the heating season is from January to March and from November to December, and the cooling season is from June to August. In Lanzhou, the heating season is from November to December and January to March, and there is no air conditioning demand in Lanzhou.

Figure 5 present the monthly transmission load in three cities. Positive values indicate heat transfer to indoors, while negative values indicate heat transfer to the outside. It can be found that heat transmission was susceptible to seasonal factors and geographical locations. The apex value of cooling demand in Shanghai was in August, which was 10.3 MJ/m^2, and the apex value of heating demand in Shanghai was in January, which was 5.5 MJ/m^2. The peak cooling demand in Beijing was in August, which was 7.3 MJ/m^2, and the peak heating demand in Beijing was in December, which was 7.6 MJ/m^2. The peak heating demand in Lanzhou was in January, which was 7.1 MJ/m^2. It can also be observed that in December and February in Shanghai and in March in Beijing and Lanzhou, the heat transfer value is positive, and that means that heat gain through the ASTF is more than the heating load. This will help reduce heating energy consumption in winter. When we look at the heat transmission of the three cities, it can also be seen that the cooling load of Beijing is lower than that of Shanghai in summer and the heat load of Beijing is higher than that of Shanghai. That is because Beijing is located at a higher latitude, with higher solar radiation on the ASTF surface, but with lower ambient temperature, which makes greater heat loss in the ASTF system. The heating demand of Lanzhou is the largest, as it is located in the cold climate zone as in Beijing and lower altitude than Beijing, which makes its ambient temperature as low as Beijing but the solar energy received by the ASTF is lower than Beijing.

Figure 6 is the comparison of monthly heat gain of hot water and monthly average thermal efficiency in Beijing, Shanghai and Lanzhou. The mean annual efficiency of the cities is 42.0%, 38.2% and 40.6%, respectively. The heat gain of hot water generation in these cities is 1640.6 MJ, 1194.4 MJ and 1537.0 MJ, respectively. The thermal efficiency of the ASTF has the highest value in Beijing, and the hot water generation of the system is also the largest in Beijing.

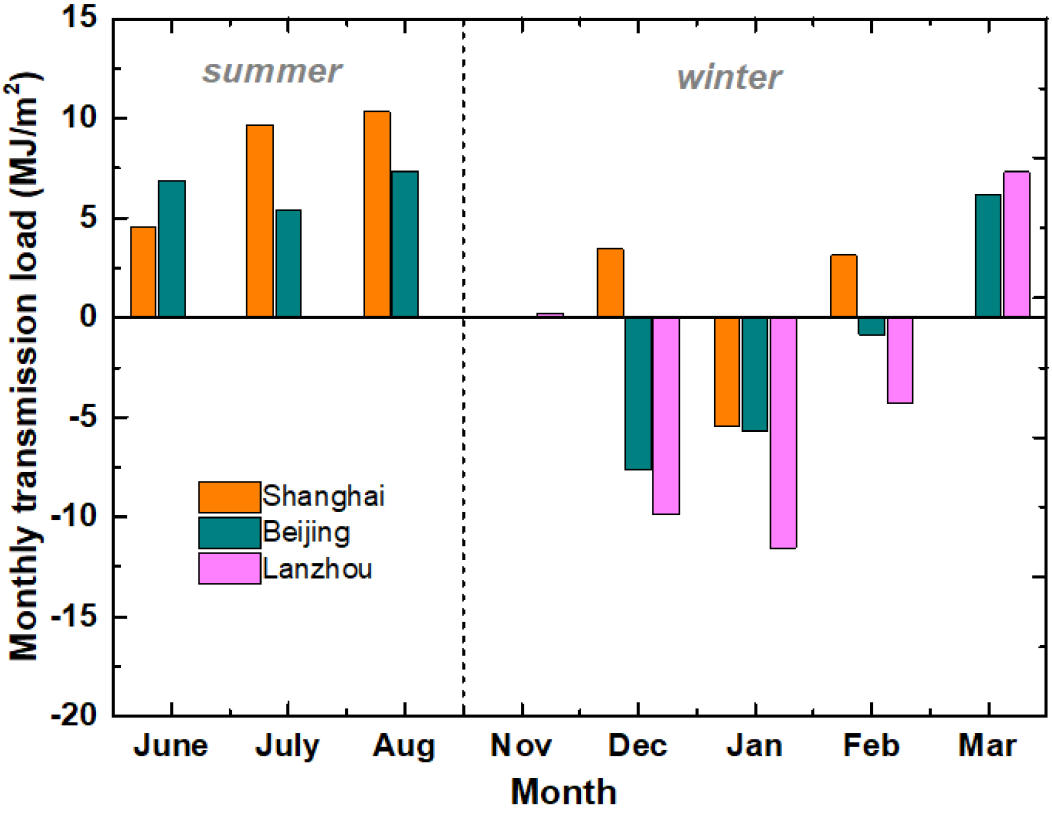

Figure 5. Monthly transmission load in three cities.

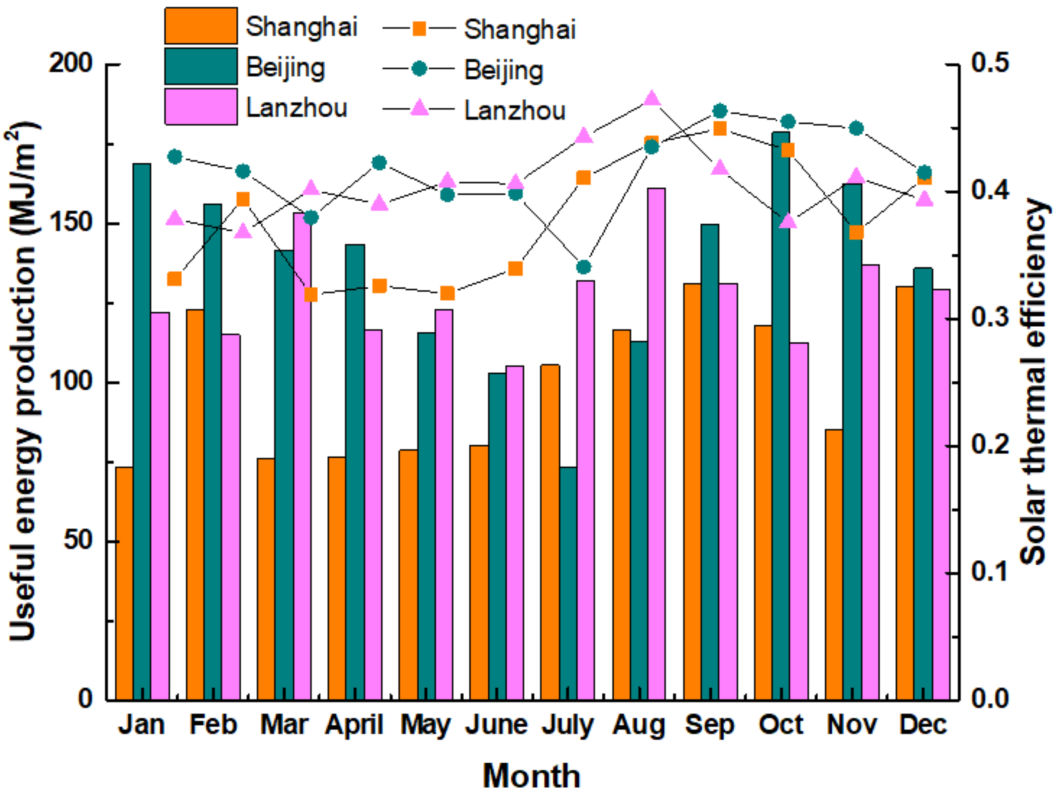

Figure 6. Monthly hot water supply in three cities.

3.2. Performance Comparison between the ASTF and Concrete Wall

To further research the energy performance of the ASTF, a traditional wall (Figure 7b) is introduced to compare it. For the traditional wall, it is simplified into a four-layer structure with a concrete layer sandwiched between the cement mortar, and the outermost layer is the insulation. The nominal heat transfer coefficient is 1.0 W/ $(m^2 \cdot K)$. The physical parameters of the different layers are presented in Table 6.

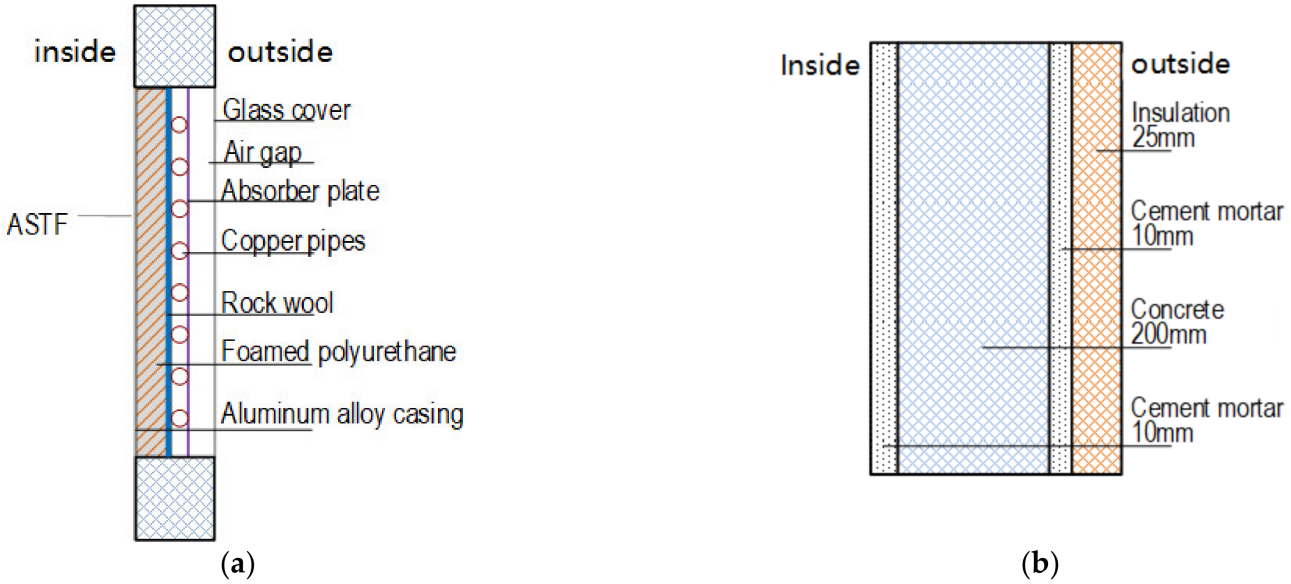

Figure 7. Structure comparison of ASTF and traditional wall (**a**) ASTF (**b**) traditional wall.

Table 6. Physical properties of traditional wall layers.

Material	Concrete	Cement Mortar	Insulation
Thermal conductivity $k(W/(m^2 \cdot K))$	1.74	0.93	0.03
Density $\rho(kg/m^3)$	2400	1800	22.5
Heat capacity $C(J/(kg \cdot K))$	920	1050	1470

Figure 8 demonstrate the contrasting results of the annual energy performance of the traditional wall and the ASTF. Obviously, the ASTF is more energy-saving. In the summer in Shanghai and Beijing, the cooling load of the traditional wall is 29.3 MJ/m^2 and 25.46 MJ/m^2 respectively, while that of the ASTF is 24.5 MJ/m^2 and 19.6 MJ/m^2, which saves 16.4% and 23.0% of cooling energy consumption, respectively. In the winter in Shanghai and Beijing, the heating load of the traditional wall is 48.3 MJ/m^2 and 103.3 MJ/m^2, while that of the ASTF is −1.1 MJ/m^2 and 7.9 MJ/m^2, which saves 102.3% and 92.4% of heating energy consumption, respectively. In the winter in Lanzhou, the heat load of the traditional wall is 134.4 MJ/m^2 while that of the ASTF is 13.7 MJ/m^2, which saves 89.8% of heating energy consumption.

3.3. 3E Assessment

3.3.1. Primary Energy Saving

The primary energy consumption in summer and winter of the traditional wall and the ASTF are demonstrated in Figure 9 for comparison. Obviously, the primary energy consumption of the ASTF is significantly reduced, especially in winter. In winter in Shanghai, the ASTF supplies to the building instead of consuming heat energy. In winter in Beijing and Lanzhou, primary energy consumption is decreased by 92.3% and 74.7%, respectively. Figure 10 show the total primary energy saving of the ASTF and the ASTF system. Primary energy saving through ASTF accounts for 5.8%, 7.2% and 11.4% of the

total primary energy savings for Shanghai, Beijing and Lanzhou, respectively. It can be concluded that the ASTF system contributes more where there is more heating demand.

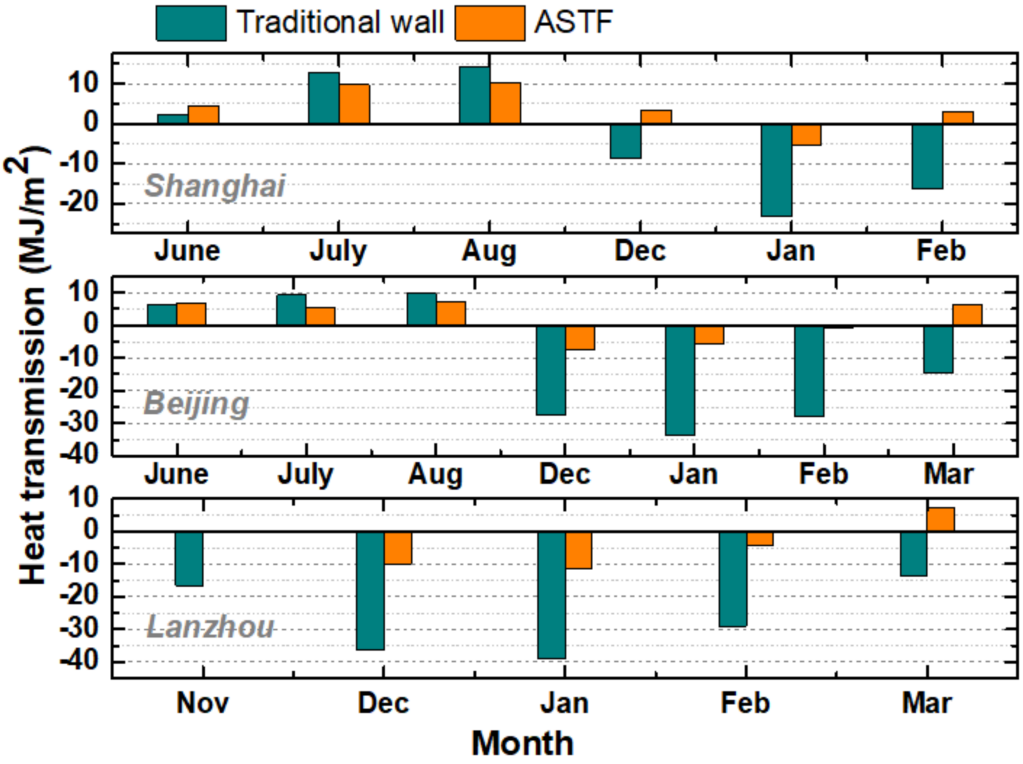

Figure 8. Heat transmission load of the ASTF in three typical cities.

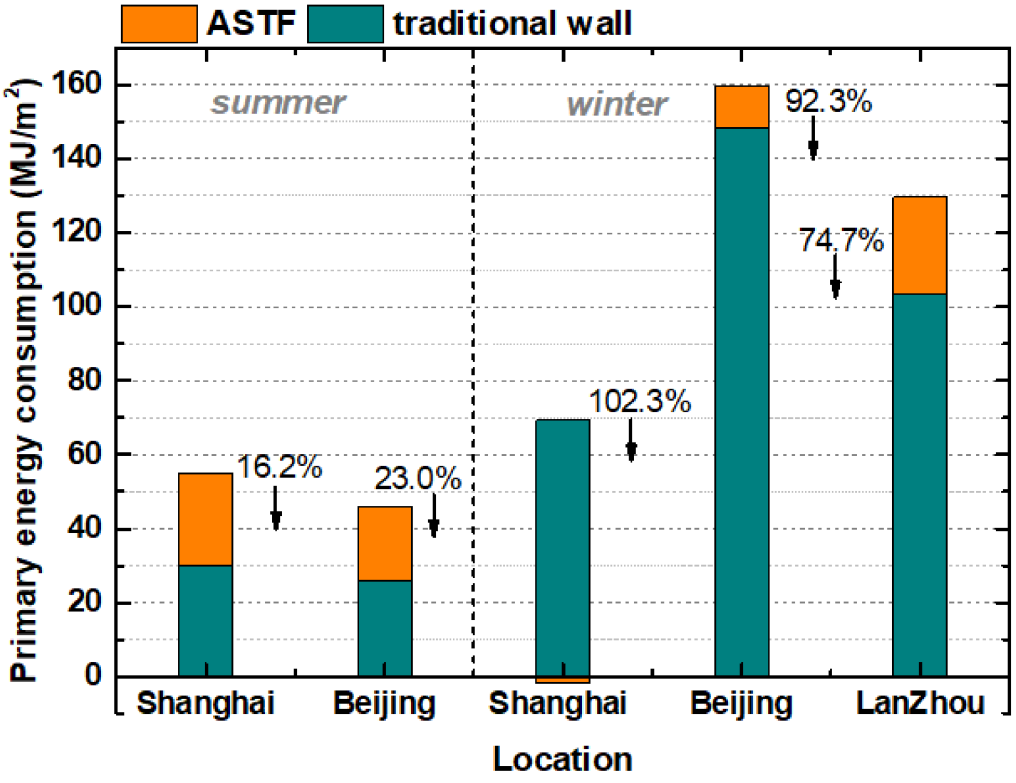

Figure 9. Comparison of primary energy consumption.

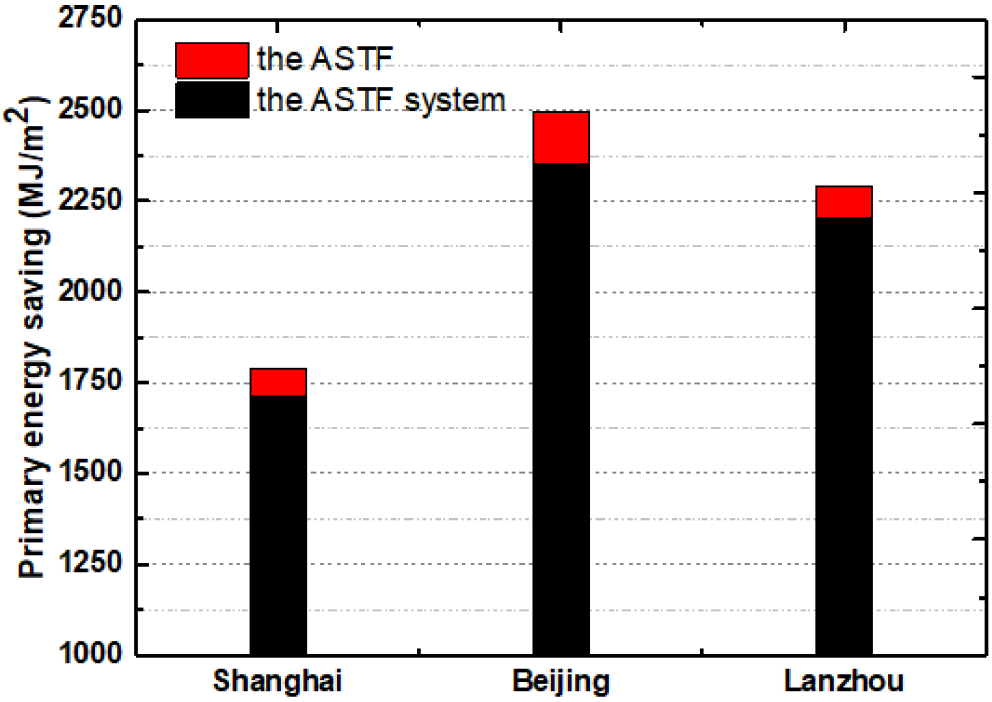

Figure 10. Primary energy savings in three cities.

3.3.2. Life-Cycle Savings

The life-cycle savings of the ASTF system are 1232.7 RMB/m^2, 2065.8 RMB/m^2 and 1923.4 RMB/m^2 for Shanghai, Beijing and Lanzhou, respectively.

Figure 11 show the net present values (NPV) from the 1st year to the 20th year. The NPV change from negative to positive at the time of the ninth year, sixth year and sixth year for Shanghai, Beijing and Lanzhou, respectively. Therefore, the discounted payback period of the ASTF system is 9 years, 6 years and 6 years for Shanghai, Beijing and Lanzhou, respectively.

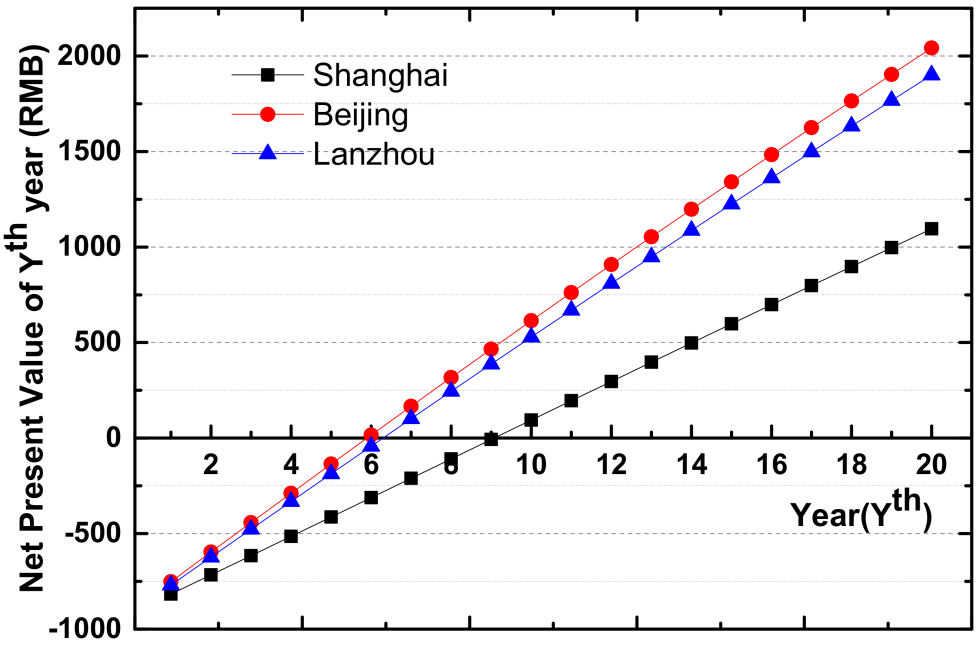

Figure 11. Net present value (NPV) at the time of Yth year over 20 years.

3.3.3. CO_2 Emission Reduction

Figure 12 show the annual total CO_2 emission reduction through the ASTF and the ASTF system.

The yearly CO_2 reduction through the ASTF is 6.57 kg/m^2, 6.15 kg/m^2 and 6.98 kg/m^2 for Shanghai, Beijing and Lanzhou, respectively.

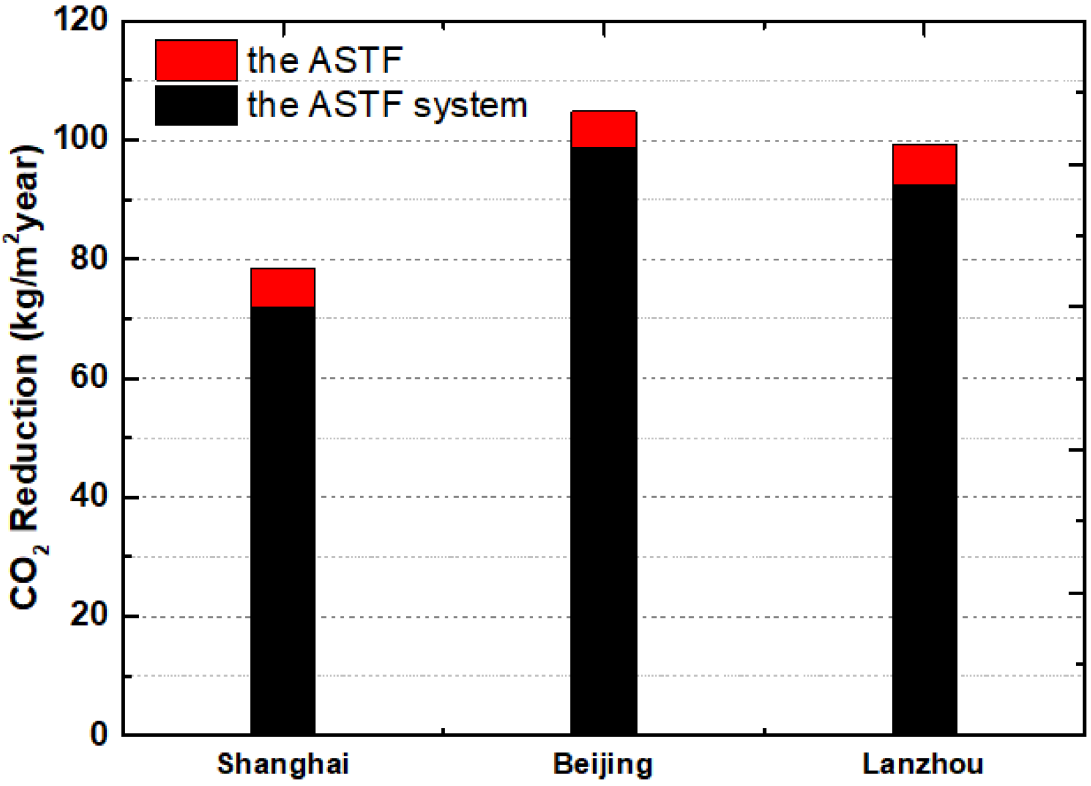

Figure 12. Annual CO_2 emission reduction.

3.4. Parametric Analysis

To further explore the better performance of the ASTF in different climate zones, the impact of some configuration parameters such as the tank volume to collector area ratio and insulation thickness on primary energy consumption are put forward.

3.4.1. Effect of Tank Volume to Collector Area Ratio

Figure 13 show the primary energy consumption of the ASTF under different ratios of water tank volume to the ASTF module area. The reason why this ratio is discussed in this section is that it affects the thermal performance of the ASTF and the ASTF system by affecting the fluid temperature and pump operation.

As is shown in Figure 13, the change range of the ratio is set from 30 to 70 L/m^2, of which 50 L/m^2 is the ratio used in the experimental system. It can be seen that with the increase in the ratio, the primary energy consumption of the ASTF in these three cities all decreased in summer but increased in winter. Additionally, with the increase in the ratio, the total yearly consumption of the ASTF in Beijing and Lanzhou both rise, while in Shanghai, it increases at first and then decreases.

3.4.2. Effect of Insulation Thickness

For traditional walls, heat transfer to the interior increases with increasing solar radiation, which is beneficial in winter while increasing the air conditioning load in summer. However, the ASTF is different. As a part of the solar heating system, the thermal performance of the ASTF is not only affected by environmental temperature and solar radiation

but also affected by the working condition of the system, which makes the problem more complicated. Therefore, studying the effects of insulation thickness on the energy performance of the ASTF has great significance for the application of the ASTF in different areas.

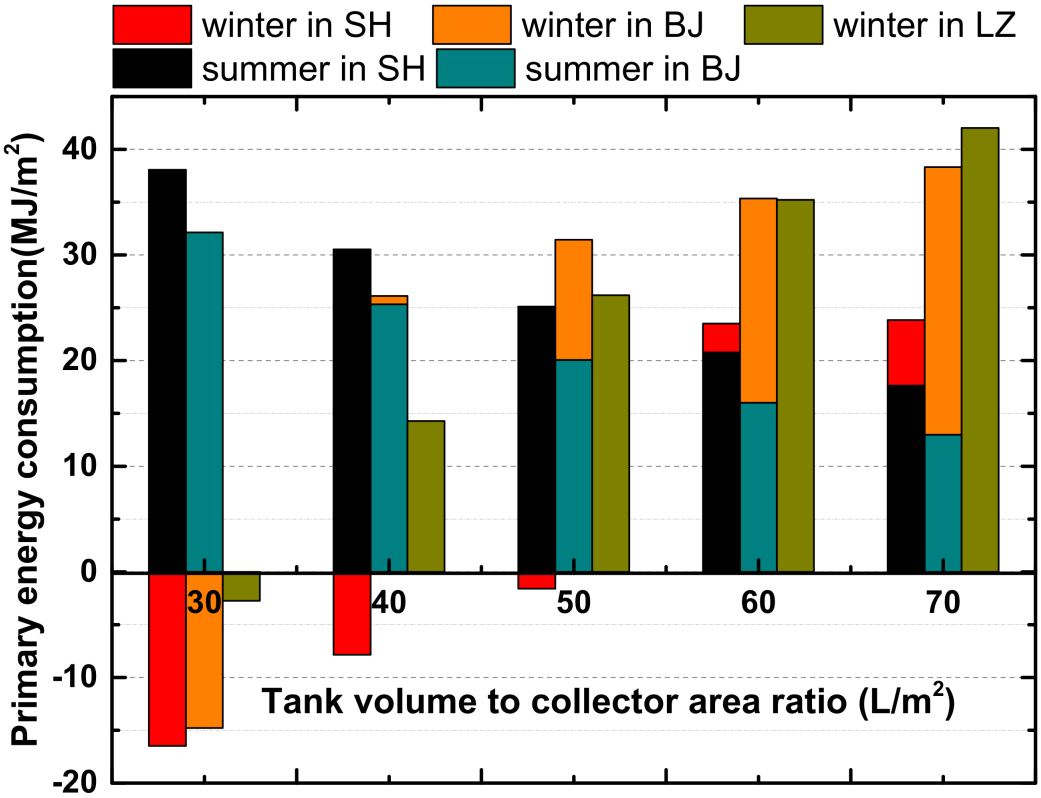

Figure 13. Primary energy consumption under different tank volume to collector area ratios.

Figure 14 display the change of annual primary energy consumption of the ASTF with insulation thickness, and negative primary energy consumption in winter means heating supply. The insulation thickness is set from 15 mm to 55 mm, of which 25 mm is used in the experimental system. It is easy to observe that when insulation thickness increases, primary energy consumed by the ASTF in the three cities are all reduced in summer while that is the opposite in winter. For Shanghai, primary energy consumption in winter is increasing, while for Beijing and Lanzhou, primary energy consumption first increases and then decreases with the variation of the insulation thickness. That is because when the insulation layer thickness is less than 0.035 m, with the change of the insulation layer thickness, the reduction of the heat conduction through the ASTF is less than that of heat supply by the ASTF. When the insulation layer thickness is more than 0.035 m, the heat conduction through the wall is dominant. A conclusion can be drawn from the results described above that the increase in the insulation layer thickness reduces the cooling load while decreasing the heating supply in winter. The value is best set according to the yearly total energy consumption or heating and cooling demand in different places.

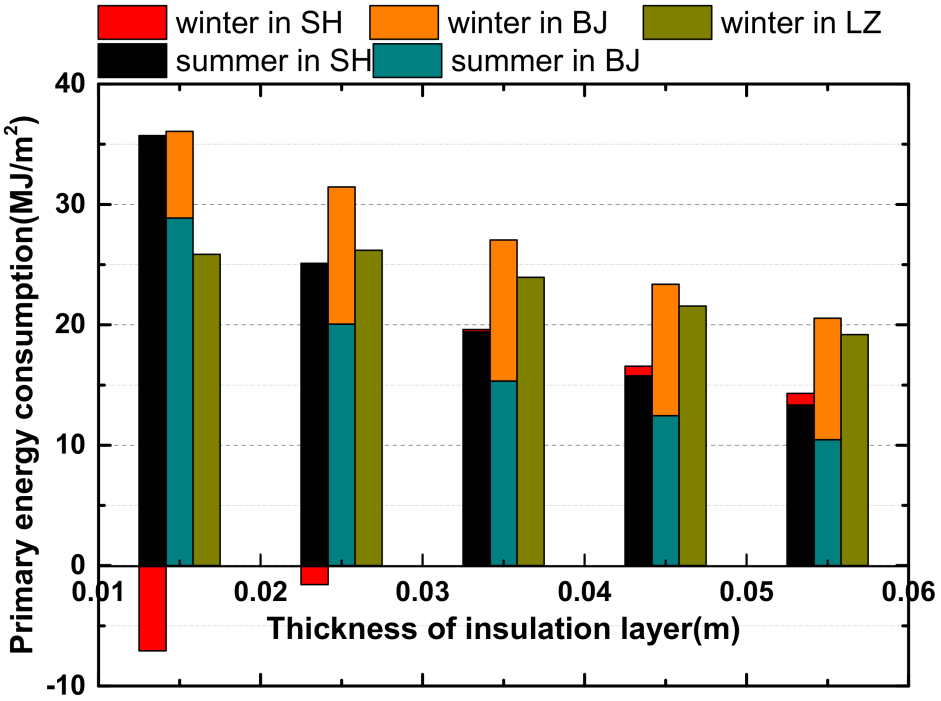

Figure 14. Variation of primary energy consumption with insulation layer thickness.

4. Conclusions

This paper proposed a dual-functional solar thermal façade system. The annual thermal performance of a bifunctional active solar thermal façade system was theoretically and experimentally studied. With the validated mathematical model, the energy, economic and environmental performance of the active solar thermal façade system in different climate zones was analyzed. The influence of different parameters on energy performance was investigated. Despite its limitations, this study undoubtedly increases our understanding of the following points:

(1) Heat transmission was affected by seasons and climate zones. The apex value of the cooling demand in Shanghai was in August, which was 10.3 MJ/m^2, and the apex value of the heating demand in Shanghai was in January, which was 5.5 MJ/m^2. The peak cooling demand in Beijing was in August, which was 7.3 MJ/m^2, and the peak heating demand in Beijing was in December, which was 7.6 MJ/m^2. The peak heating demand in Lanzhou was in January, which was 11.5 MJ/m^2;

(2) Compared with the traditional wall, the active solar thermal façade saved 16.4% and 23.0% of cooling energy consumption and 102.3% and 92.4% of heating energy consumption for Shanghai and Beijing, respectively. Additionally, it saved 74.7% of the heating energy consumption for Lanzhou;

(3) Primary energy saving through the active solar thermal façade accounts for 5.8%, 7.2% and 11.4% of the total primary energy savings for Shanghai, Beijing and Lanzhou. Life-cycle savings of the active solar thermal façade system are 1232.7 RMB/m^2, 2065.8 RMB/m^2 and 1932.4 RMB/m^2 for Shanghai, Beijing and Lanzhou, respectively.

(4) Increasing tank volume to collector area ratio or insulation layer thickness will decrease cooling energy consumption while reducing heating supply in winter;

In spite of the considerable achievements of the past few years, there is still a long way to go for the active solar thermal façade system to large-scale application. It is expected that this study will be beneficial to project engineers. However, there are still no field-accepted guidelines on how to make the active solar thermal façade system economical and energy-saving at the same time. In future work, multi-objective optimization will be made on the active solar thermal façade system to explore its better application in more different places.

Author Contributions: Data curation, R.L.; Funding acquisition, G.C.; Investigation, R.L.; Methodology, R.L.; Software, R.L.; Visualization, G.C.; Writing–Original draft, R.L. All authors have read and agreed to the published version of the manuscript.

Funding: This research received no external funding.

Conflicts of Interest: The authors declare no conflict of interest.

Abbreviation

Nomenclature

A	Area (m^2)
C	Specific heat capacity (J/(kg·K))
D_o	Outer diameter (m)
D_i	Inner diameter (m)
G_t	Solar radiation flux on tilt surface (W/m^2)
U	Heat loss coefficient ($W/(m^2 \cdot K)$)
V	Volume (m^3)
W_o	Distance between tubes (m)
W	Width of the ASTF module (m)
h	Heat transfer coefficient ($W/(m^2 \cdot K)$)
I	Investment
q	Heat flux (W/m^2)
t	Temperature (K)
m	Mass flow rate of fluid (kg/s)
v	wind velocity (m/s)
R	Thermal resistance ($m^2 \cdot K/W$)
Z	Initial investment of equipment
r_i	Inflation rate
r_d	Discount rate
r_r	Real floating interest rate

Greek symbols

α	Absorption rate
ρ	Density (kg/m^3)
ε	Emissivity
δ	Thickness, m
λ	Thermal conductivity (W/(m·K))
Δ	Difference
τ	Time, s; transmittance
σ	Boltzmann constant

Subscripts

a	Ambient air
b	Inner wall
r	Radiation
c	Convection
g	Glass cover
u	Useful
p	Absorber plate
w	Wall
ins	Insulation
f	Fluid medium
e	Emittance
s	Sky
i	Indoor room
st	Storage tank
ex	Heat exchanger
$pump$	Water pump

ctrl	Controller
d	Daily
m	Monthly
gas	Gas
Abbreviation	
ASTF	Active solar thermal façade
CE	CO_2 emission
PES	Primary energy saving
LC	Life-cycle savings
REF	Reference system
PWF	Present worth factor
NPV	Net present value

References

1. U.S. Energy Information Administration (EIA). *International Energy Outlook 2013*; EIA: Washington, DC, USA, 2014.
2. Li, J.; Colombier, M. Managing carbon emissions in China through building energy efficiency. *J. Environ. Manag.* **2009**, *90*, 2436–2447. [CrossRef] [PubMed]
3. China Association of Building Energy Efficiency. China building energy consumption research Report 2020. *Build. Energy Effic.* **2021**, *49*, 30–39.
4. Wang, L. *Building Energy Efficiency*; China Architecture& Building Press: Beijing, China, 2004. (In Chinese)
5. Deng, C.; Chen, F. Preliminary investigation on photo-thermal performance of a novel embedded building integrated solar evacuated tube collector with compound parabolic concentrator. *Energy* **2020**, *202*, 117706. [CrossRef]
6. A, Y.; Li, N.; Long, J.; He, Y. Thermal performance of a novel solar thermal facade system in a hot-summer and cold-winter zone. *Sol. Energy* **2020**, *204*, 106–114. [CrossRef]
7. Visa, I.; Moldovan, M.; Duta, A. Novel triangle flat plate solar thermal collector for facades integration. *Renew. Energy* **2019**, *143*, 252–262. [CrossRef]
8. Ibrahim, M.; Wurtz, E.; Anger, J.; Ibrahim, O. Experimental and numerical study on a novel low temperature façade solar thermal collector to decrease the heating demands: A south-north pipe-embedded closed-water-loop system. *Sol. Energy* **2017**, *147*, 22–36. [CrossRef]
9. Gagliano, A.; Aneli, S.; Nocera, F. Analysis of the performance of a building solar thermal facade (BSTF) for domestic hot water production. *Renew. Energy* **2019**, *142*, 511–526. [CrossRef]
10. Gagliano, A.; Tina, G.M.; Aneli, S.; Chemisana, D. Analysis of the performances of a building-integrated PV/Thermal system. *J. Clean. Prod.* **2021**, *320*. [CrossRef]
11. Wu, D.; Aye, L.; Yuan, Y.; Mendis, P.; Ngo, T. Comparison of optimal oriented façade integrated solar cooling systems in Australian climate zones. *Sol. Energy* **2020**, *198*, 385–398. [CrossRef]
12. Lamnatou, C.; Cristofari, C.; Chemisana, D.; Canaletti, J.L. Building-integrated solar thermal systems based on vacuum-tube technology: Critical factors focusing on life-cycle environmental profile. *Renew. Sustain. Energy Rev.* **2016**, *65*, 1199–1215. [CrossRef]
13. Harmim, A.; Boukar, M.; Amar, M.; Haida, A. Simulation and experimentation of an integrated collector storage solar water heater designed for integration into building facade. *Energy* **2019**, *166*, 59–71. [CrossRef]
14. Motte, F.; Notton, G.; Cristofari, C.; Canaletti, J.-L. Design and modelling of a new patented thermal solar collector with high building integration. *Appl. Energy* **2013**, *102*, 631–639. [CrossRef]
15. O'Hegarty, R.; Kinnane, O.; McCormack, S.J. Parametric investigation of concrete solar collectors for façade integration. *Sol. Energy* **2017**, *153*, 396–413. [CrossRef]
16. Jia, H.; Cheng, X.; Zhu, J.; Li, Z.; Guo, J. Mathematical and experimental analysis on solar thermal energy harvesting performance of the textile-based solar thermal energy collector. *Renew. Energy* **2018**, *129*, 553–560. [CrossRef]
17. Yang, Y.; Wang, Q.; Xiu, D.; Zhao, Z.; Sun, Q. A building integrated solar collector: All-ceramic solar collector. *Energy Build* **2013**, *62*, 15–17. [CrossRef]
18. Mertin, S.; Hody-Le Caër, V.; Joly, M.; Mack, I.; Oelhafen, P.; Scartezzini, J.-L.; Schüler, A. Reactively sputtered coatings on architectural glazing for coloured active solar thermal façades. *Energy Build* **2014**, *68*, 764–770. [CrossRef]
19. Matuska, T.; Sourek, B. Façade solar collectors. *Sol. Energy* **2006**, *80*, 1443–1452. [CrossRef]
20. Ji, J.; Chow, T.-T.; He, W. Dynamic performance of hybrid photovoltaic/thermal collector wall in Hong Kong. *Build. Environ* **2003**, *38*, 1327–1334. [CrossRef]
21. Swinbank, W.C. Long-wave radiation from clear skies. *Q. J. R. Meteorol. Soc.* **1963**, *89*, 339–348. [CrossRef]
22. Watmuff, J.H.; Charters, W.W.S.; Proctor, D. Solar and Wind Induced External Coefficients for Solar Collectors. *COMPLES* **1977**, *2*, 56.
23. Holman, J.P. *Heat Transfer*; metric editions ed.; McGraw-Hill: Singapore, 1989.
24. Dittus, F.W.; Boelter, L.M.K. Heat transfer in automobile radiators of the tubular type. *Int. Commun. Heat Mass Transf.* **1985**, *12*, 3–22. [CrossRef]

25. Al-Sanea, S.A.; Zedan, M.F.; Al-Hussain, S.N. Effect of thermal mass on performance of insulated building walls and the concept of energy savings potential. *Appl. Energy* **2012**, *89*, 430–442. [CrossRef]
26. Yang, S. *Progress on the Basic Law of Natural Convection Heat Transfer*; Higher Education Press: Beijing, China, 1995.
27. Li, R.; Cui, G.M. Thermal performance and parametric analysis of a dual-function active solar thermal façade system. *J. Build. Eng.* **2021**, *42*, 103042. [CrossRef]
28. Troup, L.N.; Fannon, D.J.; Eckelman, M.J. Spatio-temporal changes among site-to-source conversion factors for building energy modeling. *Energy Build* **2020**, *213*. [CrossRef]
29. Duffie, J.A.; Beckman, W.A. *Beckman, Solar Engineering of Thermal Processes*; Wiley: New York, NY, USA, 2013.
30. Li, R.; Dai, Y.; Cui, G. Multi-objective optimization of solar powered adsorption chiller combined with river water heat pump system for air conditioning and space heating application. *Energy* **2019**, *189*, 116141. [CrossRef]
31. Zheng, R. *Engineering Technical Manual of Solar Hot Water System in Civil Buildings*; Chemical Industry Press: Beijing, China, 2011. (In Chinese)